ARTICLE

Received 00th January 20xx, Accepted 00th January 20xx

DOI: 10.1039/x0xx00000x

Rapid and specific detection of intact viral particles using functionalized microslit silicon membranes as a fouling-based sensor

Michael E. Klaczko^a, Kilean Lucas^b, Alec T. Salminen^b, Molly C. McCloskey^b, Baturay Ozgurun^b, Brian M. Ward^c, Jonathan Flax^d and James L. McGrath^b

The COVID-19 pandemic demonstrated the public health benefits of reliable and accessible point-of-care (POC) diagnostic tests for viral infections. Despite the rapid development of gold-standard reverse transcription polymerase chain reaction (RT-PCR) assays for SARS-CoV-2 only weeks into the pandemic, global demand created logistical challenges that delayed access to testing for months and helped fuel the spread of COVID-19. Additionally, the extreme sensitivity of RT-PCR had a costly downside as the tests could not differentiate between patients with active infection and those who were no longer infectious but still shedding viral genomes. To address these issues for the future, we propose a novel membrane-based sensor that only detects intact virions. The sensor combines affinity and size based detection on a membrane-based sensor and does not require external power to operate or read. Specifically, the presence of intact virions, but not viral debris, fouls the membrane and triggers a macroscopically visible hydraulic switch after injection of a 40µL sample with a pipette. The device, which we call the µSiM-DX (microfluidic device featuring a silicon membrane for diagnostics), features a biotincoated microslit membrane with pores ~2-3X larger than the intact virus. Streptavidin-conjugated antibody recognizing viral $surface\ proteins\ are\ incubated\ with\ the\ sample\ for\ ``1\ hour\ prior\ to\ injection\ into\ the\ device,\ and\ positive/negative\ results$ are obtained within ten seconds of sample injection. Proof-of-principle tests have been performed using preparations of vaccinia virus. After optimizing slit pore sizes and porous membrane area, the fouling-based sensor exhibits 100% specificity and 97% sensitivity for vaccinia virus (n = 62). Moreover, the dynamic range of the sensor extends at least from 10^{5.9} virions/mL to $10^{10.4}$ virions/mL covering the range of mean viral loads in symptomatic COVID-19 patients ($10^{5.6}$ - 10^7 RNA copies/mL). Forthcoming work will test the ability of our sensor to perform similarly in biological fluids and with SARS-CoV-2, to fully test the potential of a membrane fouling-based sensor to serve as a PCR-free alternative for POC containment efforts in the spread of infectious disease.

Introduction

Reliable, accurate and accessible tests for viral infection have been one of the most important tools in efforts to control the spread of COVID-19¹⁻⁵. Reverse transcription polymerase chain reaction (RT-PCR), long the gold-standard in diagnostic testing for infection, was established for the SARS-CoV-2 virus only weeks into the⁶⁻⁸. While highly accurate, accessibility quickly became an issue as global demand for testing grew and the relationship between testing and quarantine requirements remained uncertain. This created a shortage of RT-PCR reagents from manufacturers⁹⁻¹³. In addition, the training requirements and companion instrument costs became a barrier to testing for

communities who were not equipped to do RT-PCR. This led to quality control issues which increased the likelihood of false negatives and false positives¹⁴⁻¹⁷. Logistical challenges also delayed access to testing in poorer communities and countries, which further increased the need for global containment^{10, 18, 19}.

In addition to supply shortages, the extreme sensitivity of RT-PCR resulted in testing protocols that could not differentiate between people with active infections and those who were no longer infectious but still shedding viral genomes^{4, 20-23}. By several estimates, a previously infected person would continue to test positive using RT-PCR assays for multiple weeks after being infectious²⁴⁻²⁹. The impact of this excessive sensitivity on society was significant enough that the Centers for Disease Control and Prevention ultimately changed their quarantine guidelines for recovering SARS-CoV-2 infected patients from a testing-based criterion to a symptom-based criterion^{30, 31}. Indeed, a surprising paradigm shift emerging from COVID-19 was that accessibility to testing was more important than test sensitivity for managing disease spread³². Point-of-care (POC) diagnostic tests that detect viral antigens fit the new paradigm9, ^{10, 33, 34}. POC serological tests were also developed, but these

Electronic Supplementary Information (ESI) available: [details of any supplementary information available should be included here]. See DOI: 10.1039/x0xx00000x

a. Department of Chemistry, University of Rochester, Rochester, NY, 14627 USA.

b. Department of Biomedical Engineering, University of Rochester, Rochester, NY, 14627 USA.

^{c.} Department of Microbiology and Immunology, University of Rochester Medical Center, Rochester, NY, 14642 USA.

^d Department of Urology, University of Rochester Medical Center, Rochester, NY, 14642 USA.

lack the ability for early detection of infection and can have unacceptably low sensitivities^{10, 35-37}. Importantly, all POC tests developed during COVID-19 lack the ability to distinguish intact virus particles from viral components containing the molecular targets of the assay.

As a novel approach that could overcome some of the shortfalls seen with COVID-19 testing, we propose a sensor that reports a positive result only when surface antigens are present on a full-sized (i.e., intact) virion. While the detection of intact virus alone cannot determine infection status, an abundance of intact virus may provide strong circumstantial evidence that a patient is contagious^{31, 38-41}. In addition, the non-destructive capture of intact virus provides the opportunity for downstream analysis to be conducted, including RT-PCR, if desired. In this way, RT-PCR reagents could be limited to use with samples that have been 'pre-screened' for intact virions.

As a sensing element, we use an ultrathin (400 nm) siliconnitride membrane chip with precisely patterned pores. We have previously shown that these highly permeable 'nanomembranes' are rapidly clogged in samples containing species large enough to occupy pores⁴²⁻⁴⁵. Here, we use pores that are larger than an intact virus, but are functionalized so that the pore walls bind specific antigens on the virus surface. In this way, an intact virus is captured and clogs the membrane, while sub-viral particles and particle fragments, even if they also carry antigen, do not clog. Clogging closes the default fluidic path through a microfluidic device and reroutes fluid flow to a positive indicator. Furthermore, by changing the number of available pores, the sensitivity of the fouling-based sensor can be tuned to cover a range of viral concentrations of more than four orders-of-magnitude. As a proof-of-principle, we demonstrate this new concept in viral detection using vaccinia virus.

Experimental

μSiM-DX assembly

Acrylic microfluidic components and device assembly jigs were purchased from ALine Inc. (Rancho Dominguez, CA) to create the μ SiM-DX (**micro**fluidic device featuring a **si**licon **m**embrane for **d**iagnost**ics**). μ SiM-DXs were assembled by applying pressure to acrylic components lined with pressure sensitive adhesive onto silicon membranes aligned with the aid of the assembly jigs. Port modifications were made using PEEK tubing with an outer diameter of 1/16" and an inner diameter of 0.03" from LabSmith Inc. (TUBE-116-030P).

Membrane functionalization

Microslit (0.5 μ m and 1 μ m slit-shaped pores) silicon membranes were purchased from SiMPore Inc. (West Henrietta, NY). Slit-shaped pores were used because the long dimension increases permeability while the narrow dimension provides sized-based selectivity⁴⁶. Both formats have three 'windows' which contain the porous membrane area of the chip. These windows are housed within a thick silicon

membrane which together make a 'chip'. Before coating, chips were cleaned with piranha solution (3:1 H_2SO_4 : H_2O_2) for 30 minutes and rinsed thoroughly with deionized water. KodeTM-biotin (FSL-CONJ[1Biotin]-SC2-L1) were gifted from Kode Biotech Ltd. (Auckland, New Zealand). KodeTM-biotin solutions were made to 12.5 μ M in 70% ethanol. The cleaned chips were submerged in the KodeTM solutions for 1 minute under gentle agitation. They were then removed and heated in a 65°C oven for 40 minutes, followed by rinsing in 70% ethanol, drying, and assembly into the μ SiM-DX.

Preparation of polystyrene beads and vaccinia virus

Fluorescent streptavidin conjugated polystyrene beads were purchased from Bangs Laboratories (200 nm, CFDG001; 500 nm, CFDG003) and Spherotech Inc. (1240 nm, SVFP-1068-5). Dilutions were made in Phosphate Buffered Saline (PBS). A vaccinia virus that expresses the fluorescent protein mKate2 (exc/em-588 nm/633 nm) fused to the core protein of vaccinia virus has been previously described⁴⁷. Purified particles were ethanol fixed. Virus was diluted in PBS as necessary and stored at 4°C.

Streptavidin conjugation of vaccinia and rabbit antibody and sample pre-mixing

Hybridoma cells that produce MAb 7D11 (anti-L1) were kindly provided by Bernard Moss (NIH, Bethesda MD, USA) with permission of Alan Schmaljohn (University of Maryland, Baltimore, MA, USA). Mab 7D11 was purified and concentrated using PureProteomeTM Protein G Magnetic Beads from Millipore Sigma (LSKMAGG02)⁴⁷. Rabbit IgG Isotype Control from Thermo Fisher Scientific (02-6102, RRID AB_2532938) was used as a non-specific control. Both antibodies were streptavidin conjugated separately using the protocols and reagents provided by the Lightning Link® Streptavidin Conjugation Kit (Abcam ab102921). Streptavidin conjugated antibody was pre-mixed with vaccinia virus for 1 hour before testing to ensure ample antibody-protein interaction time. Antibody solutions were diluted in PBS as necessary and stored at 4°C.

μSiM-DX testing

Assembled $\mu SiM\text{-}DX$ devices were pre-wet by injecting PBS into the bottom channel and filling the well with $100\mu L$ of PBS. $40\mu L$ of pre-mixed sample was injected by hand using a P200 pipette at a slow, controlled rate (aiming for a total injection time of 8-10 seconds). A positive test result was indicated by the protrusion of fluid out of the indicator port, opposite of the injection port. A negative test result lacked this protrusion from the indicator port, with sample filling the well instead.

DLS measurements

A Malvern Zetasizer Nano series model number ZEN3600 was used to determine the size of vaccinia virus before and after sonication. A probe sonicator (Fisher Scientific Sonic Dismembrator Model XL2000) was used to fragment virus by inserting the probe into the vaccinia solution and sonicating at its highest setting for 10 seconds.

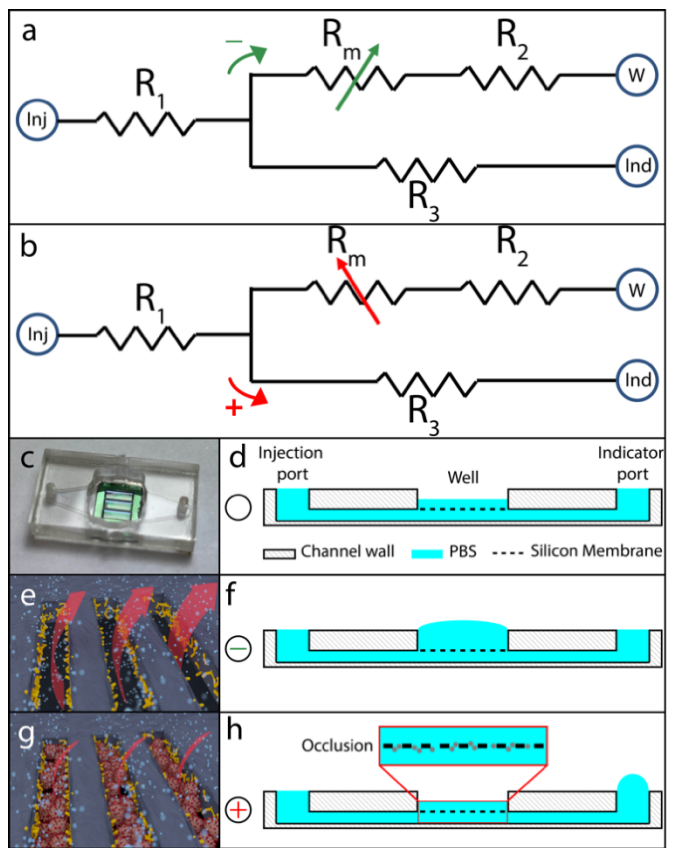


Figure 1: Concept of a fouling-based sensor for intact virus. A negative test (a) and a positive test (b) are represented in a hydraulic resistance diagram of a microfluidic device. The membranes are a variable resistor (R_m) that respond to the presence of virus, introduced through the injection port (Inj), by shunting flow to the indicator port (Ind). The design relies upon the resistance of the channels of the device (R_1 - R_3) and their outlets. The assembled μ SiM-DX (c) is pre-wet by adding PBS to the well (W) and channel to establish the test-ready state (d). Injected sample without target particles will not occlude the pores of the membranes, allowing continuous flow through the membranes (e) resulting in a negative test indicated by the well filling up (f). Injected sample with target particles will occlude the pores of the membranes, reducing flow through the membranes (g) resulting in a positive test indicated by protrusion of fluid from the indicator pore (h).

qPCR

A QuantStudioTM 3-96-well 0.2 mL Block qPCR system was used, and an established quantitative TaqMan-MGB real-time PCR assay protocol, described previously, was followed⁴⁸. DNA was isolated using the Wizard® Plus SV Minipreps DNA Purification System from Promega (A1330). Primers (Forward Primer: CGGCTAAGAGTTGCACATCCA, Reverse Primer: CTCTGCTCCATTTAGTACCGATTCT were purchased from IDT, and a minor groove binding (MGB) probe was purchased from Eurofins ([FAM]AGGACGTAGAATGATCTTGTA[MGBEQ]).

Confocal microscopy

An Andor Dragonfly Spinning Disc Confocal microscope with a Zyla 4.2 sCMOS camera was used for confocal imaging. Chips were imaged directly in the $\,\mu SiM$ -DX after testing. A 488 nm or a 637 nm laser was used to excite the fluorescent beads and a 525 nm or a 700 nm filter was used to capture emission. A 561 nm laser was used to excite the mKate2 labelled vaccinia virus and a 600 nm filter was used to capture emission.

Diagnostic Sensitivity and Specificity Calculation

Throughout this paper diagnostic sensitivity and specificity are used to gauge sensor performance. Diagnostic sensitivity was defined via the following: Diagnostic Sensitivity = True Positive / (True Positive + False Negative). Diagnostic specificity was defined via the following equation: Diagnostic Specificity = True Negative / (True Negative + False Positive)⁴⁹. Blank tests with PBS were done to test the basic function of each sensor design. To save resources, a few PBS test were done for each sensor design and extrapolated across all sensitivity and specificity tests using the same sensor design, detailed in the Supplement (Tables S.1-S.4). In an instance where no true positives were collected in testing, sensitivity was naturally 0%. If this was the case, we automatically made the corresponding specificity 0% since specificity cannot exist without sensitivity.

Single Virus Capture Analysis

Analysis of confocal images takes into account the specifications of the sCMOS camera (2048 x 2048 pixel with a pixel pitch of 6.5 μm) and a 60X/1.2NA microscope objective. This configuration makes each pixel size approximately 108 nm since it is equal to the camera pixel pitch per the magnifying power of the objective. According to Abbe's diffraction limit, the spatial resolution of the optical system is ~186 nm. Therefore, one vaccinia virus particle will occupy an area of approximately 3 x 3 pixels on the image plane. These parameters can be considered to detect single virions on the membranes. To detect single virions, the recorded image was normalized and a threshold operation was applied. A threshold value was empirically estimated by sweeping between zero and one while sequentially monitoring individual virions on the image. Once the threshold operation was complete, particles with an area of less than 3 x 3 pixels and higher than 4 x 4 pixels were eliminated since a single virion roughly covers an area between these values.

Results

System Design

Figure 1 describes the concept behind the fouling-based sensor. The microfluidic design consists of an injection port (Inj) and two outlets: the well (W) and the indicator port (Ind). Connecting these are channels with resistances, R₁-R₃, as shown. The silicon membranes occupy the path leading to the well and are shown with a variable resistance, R_m, which depends on the degree of fouling. The device (Figure 1c), which we call the μ SiM-DX, is based on the μ SiM platform originally designed for tissue chip applications^{50, 51}. In its test ready state, the bottom channel is pre-wetted, and the well is partially filled to establish fluid continuity throughout the device (Figure 1d). When sample without virus is injected, the membrane pores remain open and the flow path leading to the well is the path of lowest resistance (Figure 1a,e,f). When the pores are clogged with virus however, the membranes act as a 'resistance switch' to redirect flow to the indicator port (Figure 1b,g,h). This

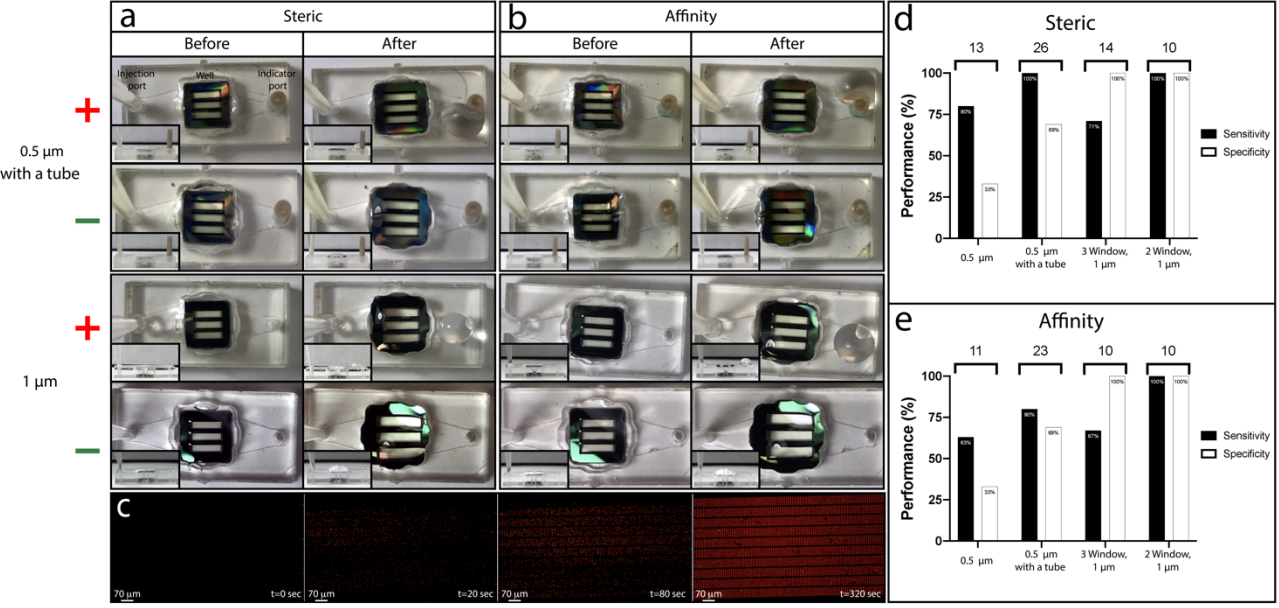


Figure 2: Optimization using steric and affinity capture of beads. Top and side views showing before and after polystyrene bead injection for steric (a) and affinity-based testing (b) in both 0.5 μm slit pores with a tube and 1 μm slit pores without a tube. A time lapse of 1.2 μm beads captured on a 1 μm slit pore membrane represents pore occlusion (c). Experiments were done using controlled microfluidic injection under a microscope and represents what capture would look like in the μSiM-DX over an 8-10 second pipette injection. After testing with PBS and bead solutions, diagnostic sensitivity and specificity can be determined for both steric capture and affinity-based capture (d,e). N values are shown above each data set. Raw data used in these calculations and the corresponding bead capture video are provided in the supplement (Table S.1, Video S.2).

produces a visual positive in the form of a bubble that protrudes from the indicator port (Figure 1h).

Sensor specificity is provided through its capture methods that depend on both affinity and size. We achieved biological affinity by conformally coating the membranes with biotin and prelabelling the sample with streptavidin-conjugated antibody that binds antigen on the virus surface. Biotin coating is achieved by dip-coating membrane chips in a solution containing an amphiphilic molecule with a terminal biotin group^{52, 53} prior to assembly into the μ SiM-DX. We found that this process results in a conformal coat of microporous silicon-nitride membranes including the pore walls (Video S.1).

Size-based selectivity is achieved with silicon nitride membranes with precisely defined slit-shaped pores⁴⁶ that are slightly larger than the intact virus. This allows for the free flow of sub-viral particles and requires capture of viruses on both walls of the pores for clogging. This choice of pore size also limits the chances of false positives due to physical capture of nonspecific particles that are larger than the pores.

We opted to establish the proof-of-concept for our new viral sensor using Vaccinia virus as a safe alternative to SARS-CoV-2. Vaccinia virus is an enveloped virus like SARS-CoV-2 but is larger (300 nm vs 65-125 nm)^{54, 55}. Despite the use of a surrogate virus for development work, we sought to design a sensor that was sensitive to the viral loads of saliva and or nasopharyngeal swabs in the range reported for SARS-CoV-2 by RT-PCR which are between 10^{5.6}-10⁷ RNA copies/mL^{56, 57}.

Demonstration of a fouling-based switch using polystyrene beads

Our earliest tests of the sensing ability of the μ SiM-DX used polystyrene beads as the simplest possible viral model. Steric capture (capture based on physical size) and affinity capture (capture based on chemical specificity) of beads allowed us to optimize the device resistances to ensure high fidelity switching behaviour at ~10⁵ bead/mL solutions, the low end of the viral concentrations we sought designs for. Both steric and affinity-based capture produced positive and negative indications with positive indications producing a bubble in the exit port as proposed (Figure 2a,b). Time lapse imaging of steric capture showed the pattern of slit pores being occupied by beads as the membrane processed more sample to become clogged (Figure 2c).

We began optimizing the design by using 500 nm beads with 0.5 μm slit pore membranes for steric capture. Note that a taper resulting from the pore-creating etching process causes the exit side of a pore to be slightly smaller (20-40 nm) than the dimension rated by the manufacturer. Shown in Figure 2d, our initial designs frequently resulted in both false positives (66% switched in PBS only solutions) and false negatives (17% failed to switch with beads in solution). False positives lower the specificity of the sensor while false negatives lower the sensitivity (see Methods for calculations).

Because the activation of the fouling-based switch requires that the open membrane resistance is much lower than the bottom channel resistance, we interpreted the sporadic performance of the sensor as an indication that the resistances were too similar. If true, this would lead to results that were sensitive to slight

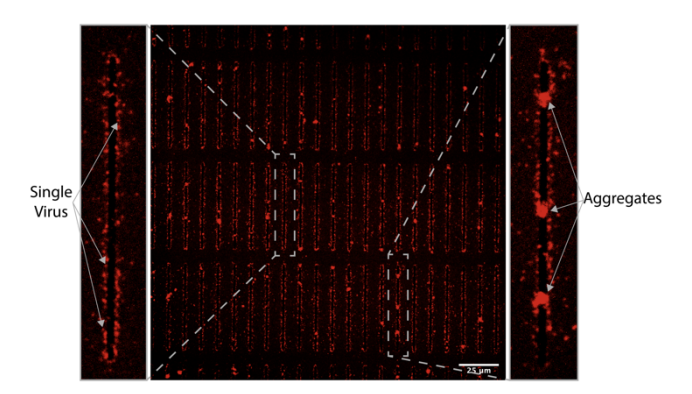


Figure 3: Confocal Imaging of Vaccina virus captured via affinity on microslit membranes. Vaccinia was observed lining the walls of the slit pores after capture. Both single virus and aggregates can be seen.

changes in injection rate and/or small variations in device-to-device geometries. We first sought to remedy the near balanced resistances by adding tubing to the indicator port as the tubing adds resistance to the bottom channel in proportion to its length. As shown in Figure 2d, the added resistance did improve performance, supporting our interpretation of the prior experiments, but still gave unsatisfactory results (69% specificity; 100% sensitivity).

We next tried to optimize device performance by lowering the membrane resistance. In these experiments, we used membranes with 1 μm slit pores and 1.2 μm beads for steric capture. Tubing was not included in this iteration, therefore the only change from the original device was a decrease in the unclogged membranes' resistance due to the use of larger pores. This design eliminated false positives to give 100% specificity but still provided frequent false negatives (Figure 2d). This suggested that we overcorrected in lowering the membrane resistance so that the membranes did not consistently clog enough to trigger a switch with 10^5 particles/mL in solution. To iterate further, we blocked one of the three membrane windows of the chip with PDMS to reduce

the overall membrane capacity. This design produced robust results in steric capture tests (100% specificity; 100% sensitivity).

Having established a working fouling-based sensor using the steric capture of beads by membrane pores, we examined the performance of the same design configurations with affinity-based capture (Figure 2e). Membrane surfaces were conformally coated with biotin (see Methods), and 200 nm streptavidin-coated beads, which are smaller than the pore sizes of both 0.5 μm and 1 μm pores, were used. With the affinity-based capture modality, the performance of the various designs were very similar to our tests using steric capture. Devices made with 0.5 μm pore sizes exhibited unacceptable sensitivity and selectivity, while the use of 1 μm pore sizes improved specificity to 100%, the sensitivity was again too low. Again, as with steric capture, limiting the membrane capacity by blocking one of the membrane windows resulted in 100% sensitivity and 100% specificity in consecutive tests.

Testing with vaccinia virus

With our prototype giving reliable detection of 10^5 bead/mL in solution, we turned to the task of detecting vaccinia virus. In these studies, membrane fouling is achieved with affinity capture of the ~300 nm virus to the walls of 1 μ m pores. While single virus capture on the opposite walls of the slit-shaped pores should leave partially opened pores, we reasoned that this still should lead to a significant increase in the membrane resistance (Calculation S.1, Figure S.1). Moreover, viruses are often aggregated in preparations and in biofluids. In this case, single capture events could recruit a cluster that spans the full width of the pore. For these reasons, we proceeded with the 1 μ m pore dimension, and we again examined the performance of chips with both 2 and 3 active membrane windows. Figure 3 shows the capture of fluorescent vaccinia virions (3 x 10^9 virions/mL) in the μ SiM-DX with 3 active windows. Fluorescent

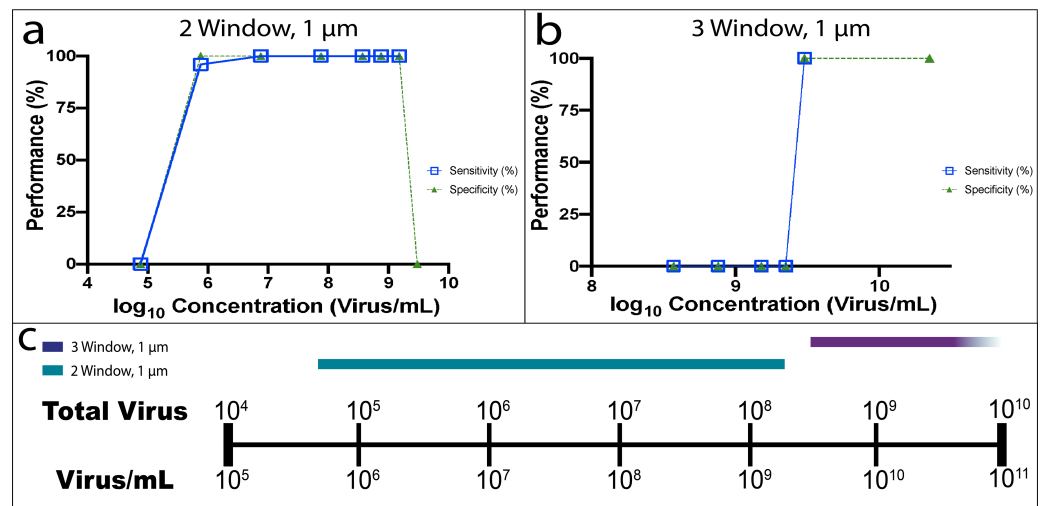


Figure 4: Detection of Vaccinia in the μSiM-DX. The dynamic range of 2 window and 3 window 1 μm slit pore μSiM-DX are detailed using diagnostic sensitivity and specificity (a,b). The dynamic range of both μSiM-DX designs are summarized (c). A vertical bar plot of this data and the raw data behind these values are provided in the supplement (Figure S.3, Table S.2).

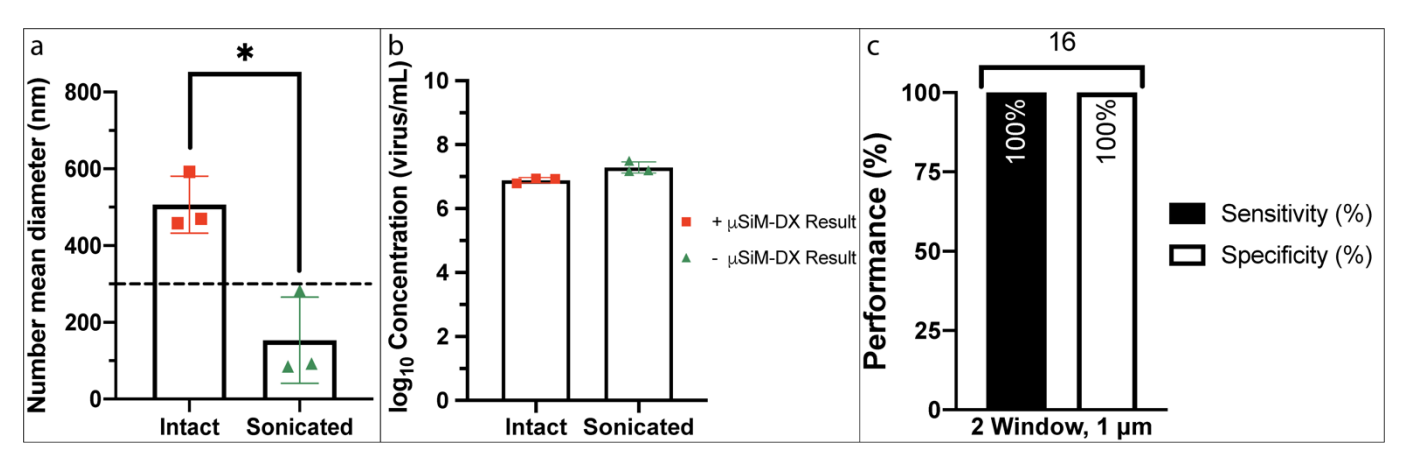


Figure 5: Analysis of Vaccinia before and after sonication. DLS data shows a significant size difference between intact and sonicated vaccinia virus according to an unpaired t test (a). The mean particle size in the native sample measures larger than single virus (300 nm denoted by the dashed line), indicating aggregation, while the sonicated sample contains mostly sub-viral particles. Error bars are generated from three technical replicates for each sample type. qPCR gives 'positive' results for both intact and sonicated samples, but the μSiM-DX only tests positive with intact virus samples (b). The 2 Slot, 1 μm μSiM-DX maintains a high diagnostic sensitivity and specificity when differentiating between intact and sonicated vaccinia (c). Testing was done at 10^{6.88}-10^{7.29} virions/mL. The N value for this range is shown above the data set. The raw data behind these values and a size distribution by number for the DLS data are provided in the supplement (Figure S.4, Table S.3).

vaccinia was observed on the edges of the slit pores under confocal microscopy, confirming specific capture to the pore walls. Given that the spatial resolution of the optical system and the pixel size of the camera are below the 300 nm size of the virus, many small particles in the image can be interpreted as single viruses (see Methods and Figure S.2). The majority of viral particles captured appear to be aggregated, including large antibody/virion aggregates that span the full width of the slit pores.

In true positive tests we incubated viral solutions with a streptavidin-conjugated antibody to the vaccinia virus surface protein L1. In true negative tests we used a streptavidin-conjugated isotype control antibody with no known affinity to vaccinia. We also studied a range of concentrations to define a dynamic range for the assay. To determine upper limits, vaccinia without antibody is used. In this scenario, the high concentration of virus simply exceeds the membrane's capacity to process the injected sample. At the limit of detection (LOD), the antibody-labelled vaccinia virus did not trigger the hydraulic switch because the concentration was too low. A detailed breakdown of the number and test type can be found in the Supplement (Table S.2).

As shown in Figure 4, both the two and three membrane window configurations displayed >96% sensitivity and 100% specificity for vaccinia over a range of concentrations that spanned more than an order-of-magnitude. Interestingly, chips with three active membrane windows and two active membrane windows had complementary dynamic ranges, which together span more than four orders of physiological virus concentrations ($10^{5.9}-10^{10.4}\,\mathrm{virions/mL}$). The 3 membrane window chips had a high LOD, failing to detect true positives at < $10^{9.5}\,\mathrm{virions/mL}$. On the other hand, the capacity of the 3 membrane window chips was so great that we did not detect an upper limit in our studies (tested to $10^{10.4}\,\mathrm{virions/mL}$). The 2 membrane window chips were able to robustly detect true

positives at 10^{9.18} virions/mL before producing false positives at 10^{9.48} virions/mL. The small gap in the dynamic range for the two chips combined, could be remedied by re-engineering the area of the three membrane window chip to be more sensitive or redesigning the 2 membrane window chips to have a slightly higher capacity. The LOD for 2 membrane window chips was 10^{5.9} virions/mL, a viral load at the low end of the range seen for symptomatic patients during the COVID-19 pandemic^{56,57}.

Differentiating between intact virus and viral debris

Following observation of robust performance over a physiological dynamic range of viral loads, we next tested if the µSiM-DX could distinguish between samples containing intact virus versus virion fragments. We fragmented virions by physically breaking down the virus using an ultrasonic probe. Dynamic light scattering measurements revealed that probe sonication reduced the average particle size in the samples from 506 nm in untreated samples to 153 nm (Figure 5a). While the nominal size of a single vaccinia virus is 300 nm⁵⁴, the 506 nm sample measurement is unsurprising given the known tendency of vaccinia to aggregate. The 153 nm measurement clearly shows that the average particle size is sub-viral following sonication. We then assayed both intact and non-intact vaccinia virus at $^{\sim}10^{7}$ virions/mL with the μ SiM-DX (1 μ m pores, 2 membrane windows) and qPCR. As shown in Figure 5b, the μSiM-DX gave positive results with intact virus samples only. By contrast, a qPCR assay detected viral genomes in both intact and sonicated samples. The qPCR results are represented as the datapoints on the bar chart. Because similar amounts of viral DNA are detected in both intact and sonicated vaccinia, the results are considered indiscernible to qPCR. The symbols of those datapoints correspond to positive or negative µSiM-DX test results. Indicated by the red squares on the chart for the intact virus datapoints, the µSiM-DX only gave positive test results with intact virus. A performance analysis using the sonicated samples as true negatives again showed the µSiM-DX with robust performance (Figure 5c). Indeed, no false positive results were recorded over 10 sonicated samples leading to a

100% sensitivity and 100% specificity for the detection of intact virus

Discussion

In this report we demonstrate the ability of a new diagnostic platform, the µSiM-DX, to detect virus accurately and reliably. The device features a membrane-based sensor that requires proper size and antigen expression to generate a response. A working dynamic range was developed for vaccinia virus on two different μSiM -DX designs differing only in the number of membranes used (2 or 3 windows). The fouling-based sensor concept was first optimized for both size and affinity-based capture using beads. For a given particle size, we demonstrated that the μSiM -DX response depends on membrane pore size and area and the relative resistances of the negative and positive flow paths. We evaluated the µSiM-DX design with diagnostic sensitivity and specificity calculations in both bead and virus testing. Using membranes with complementary sensitivities and capacities, we established a dynamic range for vaccinia virus detection that was similar to the range of viral loads seen in the saliva and or nasopharyngeal swabs of SARS-CoV-2 infected patients. Importantly, the same design had the ability to reliably differentiate between samples containing intact and fragmented virus, something not possible using current testing strategies.

A sensor that can distinguish between intact and fragmented virus in a point-of-care test may help reduce the negative impacts of quarantines and isolation in future pandemics. Mental health tolls increased during the COVID-19 pandemic⁵⁸ but less so for individuals who were able to maintain social interactions⁵⁹. Economically, isolation and quarantining led to job and income losses with impacts felt long after restrictions were lifted⁶⁰. By restricting quarantines to periods of infectivity, these issues could be at least partially mitigated in the future.

While our study shows an optimized µSiM-DX can perform with greater than 97% sensitivity and 100% specificity with an intact viral target (Table S.4), there are a number of limitations that require future testing and development: 1) Currently it is unclear what the physical status of virus is in patients' who are not infectious but still measure positive by RT-PCR. Therefore, we cannot be certain that sonication creates a reasonable model of the samples in these patients; 2) Our work has been done solely with virus preparations. Testing and re-optimizing, first with biofluids and then with patient samples, must still be done to validate the design as a field-ready POC diagnostic. If false positives occur because of the complex matrix of these samples, we will explore the costs and benefits of sample preprocessing steps including filtration, dilution, and enzymatic digestion.

In addition to its potential as a stand-alone test, the $\mu SiM\text{-}DX$ could have value to pre-screen samples to identify those that are likely be positive by RT-PCR. This would reduce the use of RT-PCR reagents and help mitigate supply-chain stresses during

periods of global demand for gold-standard tests. The $\mu SiM-DX$ could also be used in POC detection of other pathogens that cause infectious disease. The fouling based sensor should be readily extended to bacteria for example, with designs that include larger pores and possibly smaller membrane areas than those used here. Because the $\mu SiM-DX$ does not require an external reader and runs on the power of a pipette, the only chemical reagent required for adaptation to a new pathogen is a streptavidin-conjugated antibody to a surface antigen. Thus, the $\mu SiM-DX$ should be more a portable and distributable solution for low-resource environments than RT-PCR, and may serve as a substitute for infectious disease testing in those environments.

In designing the $\mu SiM-DX$, we chose to functionalize the membrane pore walls with biotin, rather than with the capture antibody itself. There are several advantages to this approach. First, this approach aids in manufacturing, as the same biotin-coated $\mu SiM-DX$ should work with all similarly sized viruses. Second, by allowing the antibody to bind to the virus in solution we avoid misorientation and denaturation of antibody on the membrane surface⁶¹⁻⁶³. The third advantage of our reliance on biotin/avidin affinity to capture a viral particle on the pore wall, is that it allows for a much more rapid capture than would occur with antibody/antigen.

Biotin and avidin have an affinity of 250 fM while typical antigen-antibody affinities are measured at nM levels⁶⁴⁻⁶⁷. This difference becomes critical when considering that the virus has a very short residence time in the pores during which recognition and capture must occur. To illustrate, given that the complete injection of a 40 µL sample requires ~8 seconds, the fluid velocity in a pore will be ~11 mm/sec (Calculation S.2). Thus, the residence time in the pores of the 400 nm thick membrane will be 37 $\mu sec,$ which must be longer than the onrate with the wall for robust capture (Calculation S.2). The onrate for avidin-biotin is 1.3 x 108 M⁻¹ • sec⁻¹ while the on-rate for typical antibody-antigen is often around 1 x 10⁵ M⁻¹ • sec^{-1 66, 67}. This means that the avidin-biotin system requires only \sim 0.4 µsec while an average antibody-antigen system will require ~0.2 msec for binding inside the pore (Calculation S.2 and S.3). These calculations suggest the speed and strength of the avidin-biotin interaction is a requirement for the success we saw with the μSiM-DX. Wall-anchored capture antibodies could work only with far slower, microfluidically controlled, flows that would prohibit use as a pipette-powered POC assay.

Our testing of various prototypes revealed that the sensitivity, specificity and dynamic range of the $\mu SiM-DX$ were functions of the pore sizes, channel length, and/or membrane area. As we hypothesized in the design stages, tuning the hydraulic resistance of the membrane relative to the resistance of the exit channel was paramount to the sensor's performance. Too small or too large of a difference in these resistances would produce false positives or false negatives, respectively. The volume of sample injection can provide further control over the actuation

of the resistance switch as it is the total number of targets processed by the membrane that determines fouling, not the concentration *per se*. In other words, the same binding capacity of a membrane can be exceeded with more volume at a lower concentration or less volume at a higher concentration. In these experiments we found that 40 μ L gave a dynamic range for the μ SiM-DX that spanned viral loads in the saliva and or nasopharyngeal swabs associated with infectious COVID-19 patients. However, if more sensitivity is desired, an injection of an 80 μ L volume should lower the LOD by a factor of 2.

Because we wished to create a point-of-care test requiring only a pipette to operate, we did not control the rate of sample introduction as we could through the use of pumps. Experience taught us that aggressive injections with the pipette can cause false positives, but that slow and steady injections (around 8-10 seconds) consistently gave good results. Thus, samples must be introduced correctly to avoid variable performance in the field as a POC diagnostic. A flow rate regulating microfluidic feature or motorized injection system may be needed for mass adoption. Interestingly, every positive switch was followed by withdrawal of the protruded fluid back into the device. This indicates that either the fouled membranes remain slightly permeable or that they regain some permeability as pipette pressure is removed allowing loosely captured debris to fall from the membrane. In either case, the surface tension of the protruded droplet creates a back-pressure which passively pumps the volume from the indicator port back towards the well. The addition of a wetting indicator at the exit pore, such as colorimetric paper, would help ensure positive tests were recorded despite a receding bubble. It is worth noting that despite withstanding variable pressures throughout sample testing, the mechanical strength of the membrane is enough to withstand sample injection by hand; zero membranes broke and zero leaks were detected in all of our (more than 60) tests.

While we developed our viral sensor using the safe-to-handle vaccinia virus, applications to SARS-CoV-2 seem feasible after modifying the reagents and membrane design to achieve both size and chemical specificity. We suggest that detection of SARS-CoV-2, which is 65-125 nm in size, could be achieved by adjusting the pore sizes to 0.3 - 0.5 μm and streptavidinconjugating antibody to the S1 surface protein. Demonstrating that the μSiM -DX can distinguish between SARS-CoV-2 from other coronaviruses would be an important milestone to clear before testing in bodily fluids.

Conclusions

We have developed a POC sensor for viral particles which requires both size and surface affinity for a positive test and uses a hand pipette injection for power. We achieved this by applying a novel principle of fouling-based detection on ultrathin silicon-based membranes. The performance of our sensor has been optimized and evaluated through specificity and sensitivity assessments, first using nanoparticles, and then using vaccinia virus. We found that a membrane chip featuring

2 windows with thousands of 1 μ m slit-shaped pores functioned as a robust sensor in the μ SiM-DX. Our results show >96% diagnostic sensitivity and a 100% diagnostic specificity across all tests, including tests that used intentionally fragmented vaccinia virus as true negatives. With this work as a foundation, the μ SiM-DX platform will now be further optimized for performance in biofluids, with patient samples, and for use with a range of viral and bacterial pathogens.

Conflicts of interest

The authors declare the following competing financial interest: J.L.M. is a co-founder of SiMPore and holds an equity interest in the company. SiMPore is commercializing ultrathin silicon-based technologies including the microslit membranes used in this study.

Acknowledgements

The authors are grateful for the spirited and insightful contributions from all the attendees of the 2020 'COVID-summer Rapid Meetings.' We are especially grateful to Sam Walker, Danial Ahmad, William Houlihan, Raquel Ajalik, Fernando Ontiveros-llamas, and Elana Stennett for their work on aspects of the project that are not included here, but will be part of the future. We would wish to acknowledge and thank Dr. Stephen Henry for the gift of Kode™ Biotin molecules. This research was directly supported by a National Science Foundation Rapid Grant (CBET 2028537), and partially by IIP PFI-TT 1917902 and by a grant from the Empire State Development Fund; Division of Science, Technology and Innovation (NYSTAR COE 1689dc11).

References

- B. D. Kevadiya, J. Machhi, J. Herskovitz, M. D. Oleynikov, W. R. Blomberg, N. Bajwa, D. Soni, S. Das, M. Hasan, M. Patel, A. M. Senan, S. Gorantla, J. McMillan, B. Edagwa, R. Eisenberg, C. B. Gurumurthy, S. P. M. Reid, C. Punyadeera, L. Chang and H. E. Gendelman, *Nature materials*, 2021, 20, 593-605.
- A. La Marca, M. Capuzzo, T. Paglia, L. Roli, T. Trenti and S. M. Nelson, *Reproductive biomedicine online*, 2020, 41, 483-499.
- R. Patel, E. Babady, E. S. Theel, G. A. Storch, B. A. Pinsky, K. St George, T. C. Smith and S. Bertuzzi, mBio, 2020, 11, e00722-00720.
- C. Boodman, P. Lagacé-Wiens and J. Bullard, Canadian Medical Association journal (CMAJ), 2020, 192, E713-E713.
- O. Vandenberg, D. Martiny, O. Rochas, A. van Belkum and Z. Kozlakidis, *Nature reviews. Microbiology*, 2021, 19, 171-183
- V. Corman, O. Landt, M. Kaiser, R. Molenkamp, A. Meijer,
 D. K. Chu, T. Bleicker, S. Brunink, J. Schneider, M. L. Schmidt, D. G. Mulders, B. Haagmans, B. Veer, S. van den Brink, L. Wijsman, G. Goderski, J. L. Romette, J. Ellis, M. Zambon, M. Peiris, H. Goossens, C. Reusken, M. Koopmans

- and C. sten, Euro surveillance : bulletin européen sur les maladies transmissibles, 2020, **25**.
- 7. D. Li, J. Zhang and J. Li, *Theranostics*, 2020, **10**, 7150-7162.
- S. Bustin, A. Coward, G. Sadler, L. Teare and T. Nolan, Scientific reports (Nature Publisher Group), 2020, 10, 22214-22214.
- 9. A. Afzal, *Journal of advanced research*, 2020, **26**, 149-159.
- M. P. Cheng, J. Papenburg, M. Desjardins, S. Kanjilal, C. Quach, M. Libman, S. Dittrich and C. P. Yansouni, *Annals of internal medicine*, 2020, 172, 726-734.
- 11. T. Alaifan, A. Altamimi, D. Obeid, T. Alshehri, S. Almatrrouk and A. Albarrag, *Future virology*, 2021, **16**, 133-139.
- C. Rhee, S. Kanjilal, M. Baker and M. Klompas, Clinical infectious diseases, 2021, 72, 1467-1474.
- K. Wernike, M. Keller, F. J. Conraths, T. C. Mettenleiter, M.
 H. Groschup and M. Beer, *Transbound Emerg Dis*, 2021, 68, 253-257.
- W. Wang, Y. Xu, R. Gao, R. Lu, K. Han, G. Wu and W. Tan, JAMA: the journal of the American Medical Association, 2020, 323, 1843-1844.
- P. S. Wikramaratna, R. S. Paton, M. Ghafari and J. Lourenço, Euro surveillance: bulletin européen sur les maladies transmissibles, 2020, 25, 28.
- J. F. Huggett, V. Benes, S. A. Bustin, J. A. Garson, K. Harris, M. Kammel, M. Kubista, T. D. McHugh, J. Moran-Gilad, T. Nolan, M. W. Pfaffl, M. Salit, G. Shipley, P. M. Vallone, J. Vandesompele, C. Wittwer and H. Zeichhardt, *Clinical chemistry (Baltimore, Md.)*, 2020, 66, 1369-1372.
- 17. C. Sheridan, *Nature biotechnology*, 2020, **38**, 382-384.
- D. D. Rajgor, M. H. Lee, S. Archuleta, N. Bagdasarian and S.
 C. Quek, The Lancet infectious diseases, 2020, 20, 776-777.
- M. M. Kavanagh, N. A. Erondu, O. Tomori, V. J. Dzau, E. A. Okiro, A. Maleche, I. C. Aniebo, U. Rugege, C. B. Holmes and L. O. Gostin, *The Lancet (British edition)*, 2020, 395, 1735-1738.
- H. Lei, F. Ye, X. Liu, Z. Huang, S. Ling, Z. Jiang, J. Cheng, X. Huang, Q. Wu, S. Wu, Y. Xie, C. Xiao, D. Ye, Z. Yang, Y. Li, N. H. L. Leung, B. J. Cowling, J. He, S. S. Wong and M. Zanin, Influenza and other respiratory viruses, 2020, 14, 688-699.
- P. Y. Chia, K. K. Coleman, Y. K. Tan, S. W. X. Ong, M. Gum, S. K. Lau, X. F. Lim, A. S. Lim, S. Sutjipto, P. H. Lee, T. T. Son, B. E. Young, D. K. Milton, G. C. Gray, S. Schuster, T. Barkham, P. P. De, S. Vasoo, M. Chan, B. S. P. Ang, B. H. Tan, Y.-S. Leo, O.-T. Ng, M. S. Y. Wong, K. Marimuthu, T. Singapore Novel Coronavirus Outbreak Research and T. for the Singapore Novel Coronavirus Outbreak Research, Nature communications, 2020, 11, 2800-2800.
- J. Zhou, J. A. Otter, J. R. Price, C. Cimpeanu, D. M. Garcia, J. Kinross, P. R. Boshier, S. Mason, F. Bolt, A. H. Holmes and W. S. Barclay, *Clinical infectious diseases*, 2020, DOI: 10.1093/cid/ciaa905.
- J. Bullard, K. Dust, D. Funk, J. E. Strong, D. Alexander, L. Garnett, C. Boodman, A. Bello, A. Hedley, Z. Schiffman, K. Doan, N. Bastien, Y. Li, P. G. Van Caeseele and G. Poliquin, Clinical infectious diseases, 2020, 71, 2663-2666.
- J. An, X. Liao, T. Xiao, S. Qian, J. Yuan, H. Ye, F. Qi, C. Shen, L. Wang, Y. Liu, X. Cheng, N. Li, Q. Cai, F. Wang, J. Chen, G. Li, Q. e. Cai, Y. Liu, Y. Wang, F. Zhang, Y. Fu, Q. He, X. Tan, L. Liu and Z. Zhang, Annals of translational medicine, 2020, 8, 1084-1084.

- H. Laferl, H. Kelani, T. Seitz, B. Holzer, I. Zimpernik, A. Steinrigl, F. Schmoll, C. Wenisch and F. Allerberger, Infection 2021, 49, 95.
- L. Lan, D. Xu, G. Ye, C. Xia, S. Wang, Y. Li and H. Xu, JAMA: the journal of the American Medical Association, 2020, 323, 1502-1503.
- Y. Sohn, S. J. Jeong, W. S. Chung, J. H. Hyun, Y. J. Baek, Y. Cho, J. H. Kim, J. Y. Ahn, J. Y. Choi and J.-S. Yeom, *Journal of clinical medicine*, 2020, 9, 2924.
- R. Wölfel, V. M. Corman, W. Guggemos, M. Seilmaier, S. Zange, M. A. Müller, D. Niemeyer, T. C. Jones, P. Vollmar, C. Rothe, M. Hoelscher, T. Bleicker, S. Brünink, J. Schneider, R. Ehmann, K. Zwirglmaier, C. Drosten and C. Wendtner, Nature (London), 2020, 581, 465-469.
- V. Gniazdowski, C. P. Morris, S. Wohl, T. Mehoke, S. Ramakrishnan, P. Thielen, H. Powell, B. Smith, D. T. Armstrong, M. Herrera, C. Reifsnyder, M. Sevdali, K. C. Carroll, A. Pekosz and H. H. Mostafa, Clinical Infectious Diseases, 2020, DOI: 10.1093/cid/ciaa1616.
- 30. M. Cevik, M. Tate, O. Lloyd, A. E. Maraolo, J. Schafers and A. Ho, *The Lancet Microbe*, 2021, **2**, e13-e22.
- 31. T. Jefferson, E. A. Spencer, J. Brassey and C. Heneghan, Clinical infectious diseases, 2020, DOI: 10.1093/cid/ciaa1764.
- D. B. Larremore, B. Wilder, E. Lester, S. Shehata, J. M. Burke, J. A. Hay, M. Tambe, M. J. Mina and R. Parker, Science advances 2021, 7.
- 33. A. Premraj, A. G. Aleyas, B. Nautiyal and T. J. Rasool, *Diagnostics (Basel)*, 2020, **10**, 866.
- 34. C. Sheridan, *Nature biotechnology*, 2020, **38**, 515-518.
- 35. J. Abbasi, JAMA: the journal of the American Medical Association, 2020, 323, 1881-1883.
- 36. M. Döhla, C. Boesecke, B. Schulte, C. Diegmann, E. Sib, E. Richter, M. Eschbach-Bludau, S. Aldabbagh, B. Marx, A. M. Eis-Hübinger, R. M. Schmithausen and H. Streeck, *Public health (London)*, 2020, **182**, 170-172.
- 37. M. K. Özçürümez, A. Ambrosch, O. Frey, V. Haselmann, S. Holdenrieder, M. Kiehntopf, M. Neumaier, M. Walter, F. Wenzel, R. Wölfel, H. Renz, C.-T. F. o. t. G. S. f. C. Chemistry and M. Laboratory, *Journal of allergy and clinical immunology*, 2020, **146**, 35-43.
- L. Huang, L. Ding, J. Zhou, S. Chen, F. Chen, C. Zhao, J. Xu,
 W. Hu, J. Ji, H. Xu and G. L. Liu, *Biosensors & bioelectronics*,
 2021, 171, 112685-112685.
- A. A. Yanik, M. Huang, O. Kamohara, A. Artar, T. W. Geisbert, J. H. Connor and H. Altug, Nano letters, 2010, 10, 4962-4969.
- F. Inci, O. Tokel, S. Wang, U. A. Gurkan, S. Tasoglu, D. R. Kuritzkes and U. Demirci, ACS nano, 2013, 7, 4733-4745.
- 41. P. K. R. Kumar, Biosensors (Basel), 2016, **6**, 40.
- 42. M. Dehghani, K. Lucas, J. Flax, J. McGrath and T. Gaborski, Advanced materials technologies, 2019, **4**, 1900539-n/a.
- T. R. Gaborski, J. L. Snyder, C. C. Striemer, D. Z. Fang, M. Hoffman, P. M. Fauchet and J. L. McGrath, ACS nano, 2010,
 4. 6973-6981.
- 44. C. C. Striemer, P. M. Fauchet, T. R. Gaborski and J. L. McGrath, *Nature (London)*, 2007, **445**, 749-753.
- J. D. Winans, K. J. P. Smith, T. R. Gaborski, J. A. Roussie and J. L. McGrath, *Journal of membrane science*, 2016, 499, 282-289.

62.

63.

65.

66.

67.

- E. Wright, J. J. Miller, M. Csordas, A. R. Gosselin, J. A. Carter,
 J. L. McGrath, D. R. Latulippe and J. A. Roussie,
 Biotechnology and bioengineering, 2020, 117, 879-885.
- 47. N. J. Parekh, T. E. Krouse, I. E. Reider, R. P. Hobbs, B. M. Ward and C. C. Norbury, *PLoS pathogens*, 2019, **15**.
- 48. J. L. Baker and B. M. Ward, *Journal of virological methods*, 2014, **196**, 126-132.
- R. Parikh, A. Mathai, S. Parikh, G. Chandra Sekhar and R. Thomas, *Indian journal of ophthalmology*, 2008, 56, 45-50.
- E. A. Masters, K. L. de Mesy Bentley, A. L. Gill, S. P. Hao, C.
 A. Galloway, A. T. Salminen, D. R. Guy, J. L. McGrath, H. A.
 Awad, S. R. Gill and E. M. Schwarz, *PLoS pathogens*, 2020,
 16, e1008988-e1008988.
- E. A. Masters, A. T. Salminen, S. Begolo, E. N. Luke, S. C. Barrett, C. T. Overby, A. L. Gill, K. L. de Mesy Bentley, H. A. Awad, S. R. Gill, E. M. Schwarz and J. L. McGrath, Nanomedicine, 2019, 21, 102039-102039.
- S. Henry, E. Williams, K. Barr, E. Korchagina, A. Tuzikov, N. Ilyushina, S. A. Abayzeed, K. F. Webb and N. Bovin, Scientific reports, 2018, 8, 2845-2846.
- E. Williams, K. Barr, E. Korchagina, A. Tuzikov, S. Henry and N. Bovin, *International journal of molecular sciences*, 2016, 17, 118.
- 54. L. Johnson, A. K. Gupta, A. Ghafoor, D. Akin and R. Bashir, Sensors and actuators. B, Chemical, 2006, **115**, 189-197.
- 55. I. Astuti and Ysrafil, *Diabetes & metabolic syndrome clinical research & reviews*, 2020, **14**, 407-412.
- 56. T. C. Jones, G. Biele, B. Mühlemann, T. Veith, J. Schneider, J. Beheim-Schwarzbach, T. Bleicker, J. Tesch, M. L. Schmidt, L. E. Sander, F. Kurth, P. Menzel, R. Schwarzer, M. Zuchowski, J. Hofmann, A. Krumbholz, A. Stein, A. Edelmann, V. M. Corman and C. Drosten, Science (American Association for the Advancement of Science), 2021, DOI: 10.1126/science.abi5273, eabi5273.
- S. B. Omer, M. Simonov, J. L. Warren, B. Geng, M. Campbell, X. Jiang, A. Casanovas-Massana, R. Earnest, C. D. Odio, C. S. Dela Cruz, P. Lu, A. L. Wyllie, M. C. Muenker, J. Fournier, E. B. White, N. D. Grubaugh, M. Tokuyama, A. Venkataraman, A. J. Moore, R. Datta, S. Lapidus, A. I. Ko, D. J. Kim, S. Farhadian, C. B. F. Vogels, R. A. Martinello, A. Lu-Culligan, R. Handoko, E. Kudo, C. C. Kalinich, P. Vijayakumar, A. Iwasaki, J. Klein, M. E. Petrone, N. Naushad, M. Linehan, L. R. Sewanan, I. M. Ott, T. Mao, M. Moriyama, J. Valdez, J. E. Oh, A. Park, J. Silva, E. Song, T. Takahashi, M. Taura, O.-E. Weizman, P. Wong, Y. Yang and S. Bermejo, *The New England journal of medicine*, 2020, 383, 1283-1286.
- 58. S. Li, Y. Wang, J. Xue, N. Zhao and T. Zhu, *International journal of environmental research and public health*, 2020, **17**, 2032.
- M. Y. Ni, L. Yang, C. M. C. Leung, N. Li, X. I. Yao, Y. Wang, G.
 M. Leung, B. J. Cowling and Q. Liao, *JMIR mental health*, 2020, 7, e19009-e19009.
- M. Lenzen, M. Li, A. Malik, F. Pomponi, Y.-Y. Sun, T. Wiedmann, F. Faturay, J. Fry, B. Gallego, A. Geschke, J. Gómez-Paredes, K. Kanemoto, S. Kenway, K. Nansai, M. Prokopenko, T. Wakiyama, Y. Wang and M. Yousefzadeh, *PloS one*, 2020, 15, e0235654-e0235654.
- 61. D. B. Bush and T. A. Knotts, *The Journal of chemical physics*, 2017, **146**, 155103-155103.

- A. K. Trilling, M. M. Harmsen, V. J. B. Ruigrok, H. Zuilhof and J. Beekwilder, *Biosensors & bioelectronics*, 2013, **40**, 219-226.
- A. K. Trilling, M. J. Beekwilder and H. Zuilhof, *Analyst* (*London*), 2013, **138**, 1619-1627.
- U. Piran and W. J. Riordan, *Journal of immunological methods*, 1990, **133**, 141.
 - L. Zhang, W. Huo, Y. Gao, S. Shi and Y. Gao, *IEEE transactions on magnetics*, 2015, **51**, 1-4.
 - L. Deng, E. N. Kitova and J. S. Klassen, *Journal of the American Society for Mass Spectrometry*, 2013, **24**, 49-56.
 - J. P. Landry, Y. Ke, G.-L. Yu and X. D. Zhu, Journal of immunological methods, 2015, 417, 86-96.

Supplement

Rapid and specific detection of intact viral particles using functionalized microslit silicon membranes as a fouling-based sensor

Michael E. Klaczko, Kilean Lucas, Alec T. Salminen, Molly C. McCloskey, Baturay Ozgurun, Brian M. Ward, Jonathan Flax and James L. McGrath

Calculations

Calculation S.1: Pore Occlusion and Membrane Resistance

In order to determine how the resistance of a porous membrane changes while being occluded, the analysis below was completed on a microfluidic device that is similar to the μ SiM-DX which used a one window, 0.5 μ m slit pore membrane. In each analysis, shown in Figure S.1, all dimensions (height, width, length) but one are held constant to observe how the unconstrained dimension individually affects the total membrane resistance. In doing so, trends are observed on how the total membrane resistance is affected by each dimension. The length dimension is not analysed in this analysis since it is the least likely to clog in actual capture. Instead, total pore occlusion via the number of available pores is analysed. The resistance through each slit is modelled using the Hagen-Poiseuille equation for a rectangular shaped channel. Resistance values are determined via the following calculations with their results shown in Figure S.1. The height and width analyses assume uniform pore occlusion across every slit in the porous window, while the pore occlusion analysis assumes 100% occlusion of pores. While no analysis is perfect, together they suggest that total membrane occlusion is not necessary in order to trigger a resistance switch.

```
Dimensions:
Top channel dimensions: L = 15000 \mum, w = 1000 \mum, and h = 100 \mum
Dimensions of a single slit in the membrane: L = 0.4 \mum, w = 50 \mum, and h = 0.5 \mum
The viscosity of water at 25 °C (\mu) = 8.9x10-4 Pa•s
Number of pores in a window
Number of pores in 1 window = (Percent Porosity • Membrane Area) / Area of a single pore
    = 10% • (2100000 μm2) / 25 μm<sup>2</sup>
    = 8400 pores
Channel to the indicator port resistance (Remains constant for every analysis)
Indicator port channel resistance = (12 \bullet \mu \bullet L) / w \bullet h^3
    = 12 • 8.9E-4 Pa•s • 15000 μm / 1000 μm • (100 μm)3
    = 1.602E-7 Pa•s/μm<sup>3</sup>
Membrane Resistance (representing the minimum membrane resistance)
Resistance of a pore: R_p = (12 \mu L / (1-(0.63(h / w))) w \cdot h3
    = (12 \bullet 8.9E-4 \text{ Pa} \bullet \text{s} \bullet 0.4 \mu\text{m}) / (1- (0.63(0.5 \mu\text{m} / 50 \mu\text{m}))) \bullet (0.5 \mu\text{m}^3)
    = 6.9E-4 Pa•s/μm<sup>3</sup>
Membrane resistance: R_m = R_p / \text{(total number of pores)}
    = (6.9E-4 Pa \cdot s/\mu m^3) / 8400 pores
    = 8.189E-8 Pa \cdot s/\mu m^3
```

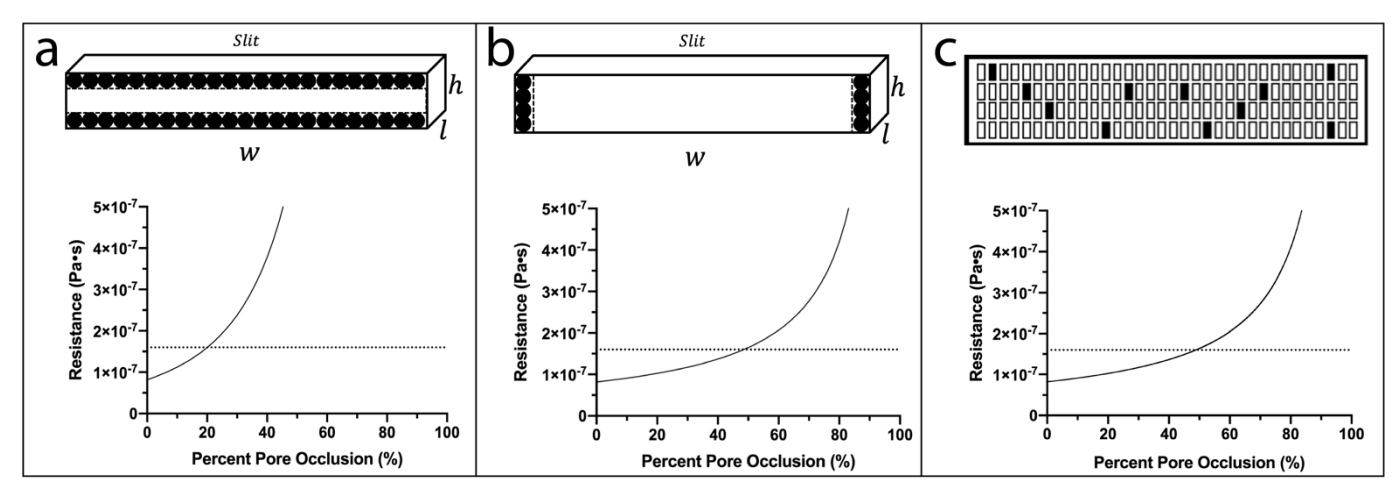


Figure S.1: Pore occlusion in a microfluidic device using a silicon nanomembrane. Three different analyses are done by decreasing the size/number of each individual pore with respect to height (a), width (b), and open pore number (c). Each is shown with an illustration of their pore occlusion and the corresponding analysis. The dashed line on each analysis represents the resistance of the channel to the indicator port.

Height Analysis

Decrease the height dimension when calculating the resistance of a pore with 0.01 μ m steps. Calculate and plot the membrane resistance as a function of percent pore occlusion. The membrane resistance crosses and becomes greater than the resistance of the indicator port channel at ~20% pore occlusion of all of the pores within the porous window.

Width Analysis

Decrease the width dimension when calculating the resistance of a pore with 1 μ m steps. Calculate and plot the membrane resistance as a function of percent pore occlusion. The membrane resistance crosses and becomes greater than the resistance of the indicator port channel at ~50% pore occlusion of all of the pores within the porous window.

Open Pore Number Analysis

Decrease the number of pores within the membrane when calculating the resistance of the membrane with 1 pore steps. Calculate and plot the membrane resistance as a function of percent pore occlusion. The membrane resistance crosses and becomes greater than the resistance of the indicator port channel at \sim 50% pore occlusion of all of the pores within the porous window.

Calculation S.2: Biotin-avidin affinity-based capture calculations

The following calculations were done to determine the amount of time an avidin bound molecule would have to stay within the pore of a silicon nanomembrane in order to have the chance to interact and bind to a biotin coating on the wall of the pore.

```
Fluid flow rate
Injection time = 8 sec
Sample volume = 40 \muL = 4E10 \mum<sup>3</sup>
Fluid flow rate = 4E10 \mu m^3 / 8 sec
    = 5E9 \mu m^3/sec
Fluid flow rate within a pore
Pore area = 1 \mu m \cdot 50 \mu m
    = 50 µm<sup>2</sup>
Number of pores in 1 window = (Percent Porosity • Membrane Area) / Area of a single pore
    = 11% • (2100000 μm<sup>2</sup>) / 50 μm<sup>2</sup>
    = 4620 pores
Number of pores in 2 windows = 4620 pores ● 2
    = 9240 pores
Total pore area across 2 windows = 9240 pores • 50 μm<sup>2</sup>
    = 462000 μm<sup>2</sup>
Fluid flow rate within a pore = (5E9 \mu m^3/sec) / 462000 \mu m^2
    = 10822.5 \, \mu m/sec \equiv 10.8 \, mm/sec
```

Journal Name **ARTICLE** Residency time within a pore Membrane thickness = $0.4 \mu m$ Residence time within a pore = $0.4 \mu m / (10822.5 \mu m/sec)$ $= 3.7E-5 \text{ sec} \equiv 37 \,\mu\text{sec}$ Streptavidin conjugated antibody concentration Streptavidin conjugated antibody concentration = 0.185 μ L * 1.06E-4 μ g/ μ L = $1.961E-5 \mu g \equiv 1.961E-11 g$ = 1.961E-11 g / 150000 g/mol = 1.307E-16 mol Sample injection volume = 0.04 L Streptavidin conjugated antibody concentration = 1.307E-16 mol / 0.04 L = 3.268F-15 M Kode™ molecule concentration across 2 windows Solid surface area of a single pore = $2(1 \mu m \cdot 0.4 \mu m) + 2(50 \mu m \cdot 0.4 \mu m)$ Total pore solid surface area across 2 windows = 40.8 μm² • 9240 pores $= 376992 \ \mu m^2 \equiv 3.76992E11 \ nm^2$ Kode[™] Biotin Spatial area (assumption) = 1 nm² Number of Kode™ molecules within the pores of 2 windows = 3.76992E11 Kode™ molecules Molecular mass of Kode[™] Biotin = 2057.34 g/mol = 3.4175E-21 g/Kode[™] molecule Mass of Kode[™] molecules within the pores of 2 windows = 3.76992E11 Kode[™] molecules • 3.4175E-21 g/Kode[™] molecule = 1.288E-9 gMoles of Kode[™] molecules within the pores of 2 windows = 1.288E-9 g / 2057.34 g/mol = 6.26E-13 mol Kode molecule size^{1, 2} = $^{\sim}$ 7 nm = 0.007 μ m Volume within the vicinity of Kode[™] molecules in a single pore = 2(1 μm • 0.4 μm • 0.007 μm) + 2(50 μm • 0.4 μm • 0.007 μm) $= 0.2856 \mu m^3$ Total volume within the vicinity of Kode™ molecules across 2 windows = 0.2856 µm³ • 9240 pores = $2638.944 \mu m^3 \equiv 2.639E-12 L$ Kode[™] molecule concentration across 2 windows = 6.26E-13 mol / 2.639E-12 L = 0.237 MConcentration of biotin-avidin complexes Streptavidin-Biotin affinity constant (K_a)³ = 2.5E13 M⁻¹ K_a = [AB] / [A] • [B] ≡ [streptavidin-biotin complexes] / [streptavidin conjugated antibody] • [Kode™ biotin molecules] $2.5E13 \text{ M}^{-1} = [AB] / 3.268E-15 \text{ M} \bullet 0.237 \text{ M}$ $2.5E13 M^{-1} = [AB] / 7.755E-16 M^{2}$ [AB] = 0.0194 M

Time required for a streptavidin-biotin complex to form

Streptavidin-Biotin on rate $(k_{on})^3 = 1.3E8 \text{ M}^{-1} \bullet \text{sec}^{-1}$

Time required for a streptavidin-biotin complex to form = 1.3E8 $M^{-1} \bullet sec^{-1} \bullet 0.0194 M$

= 2520354.7 sec $^{-1}$ = 3.968E-7 sec \equiv 0.3968 μ sec

Calculation S.3: Antibody-antigen affinity-based capture calculations (assuming similar conditions as above)

These calculations are a follow-up to Calculation S.2 which was done in order to determine the amount of time a protein antigen would have to stay within the pore of a silicon nanomembrane in order to have the chance to interact and bind to an antibody coating on the wall of the pore.

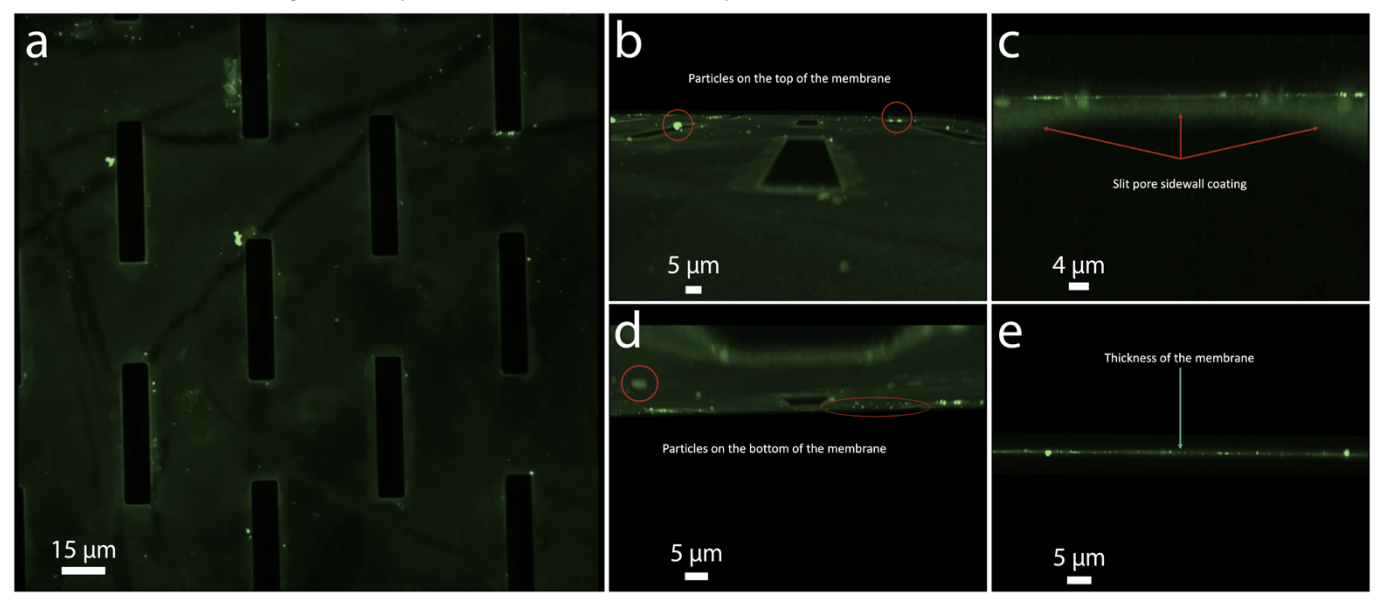
Concentration of antibody-antigen complexes Median antibody-antigen affinity constant $(K_a)^4 = 66E12 \text{ M}^{-1}$ $K_a = [AB] / [A] \bullet [B] \equiv [\text{antibody-antigen complexes}] / [\text{antigen}] \bullet [\text{antibody}]$ $66E12 \text{ M}^{-1} = [AB] / 3.268E-15 \text{ M} \bullet 0.237 \text{ M}$ $66E12 \text{ M}^{-1} = [AB] / 7.755E-16 \text{ M}^2$ [AB] = 0.0512 M

Time required for an antibody-antigen complex to form Average antibody-antigen on rate $(k_{on})^4 = 1E5M^{-1} \bullet sec^{-1}$ Time required for a protein-antibody complex to form = $1E5 M^{-1} \bullet sec^{-1} \bullet 0.0512 M$ = $5118.3 sec^{-1} = 1.954E-4 sec = 195.4 \ \mu sec$

Data

Video S.1: Kode™ FITC Conformal Coating

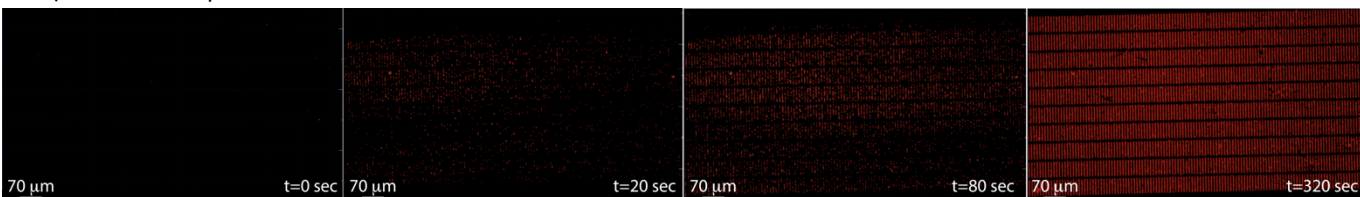
To determine whether or not KodeTM molecules were conformally coating the membranes, we coated an 8 μ m slit pore membrane with KodeTM FITC molecules. In combination with a confocal microscope, we were able to gather a z-stack which definitively showed fluorescent coating on the top of the membrane, within the pores of the membrane, and on the bottom of the membrane.



Video S.1: An 8 µm slit pore membrane coated with KodeTM FITC fluorescent molecules, imaged with an Andor Dragonfly Spinning Disc Confocal microscope. A conformal coating of the fluorescent molecules is shown perpendicular to the membrane (a). A closer look provides evidence for conformal on the top of the membrane (b), the walls of the pores (c), and the bottom of the membrane (d). The thickness of the membrane can also be shown when imaging parallel to the side of the membrane (e)

Video S.2: Bead Capture Video

Visualization of bead capture on silicon nanomembranes was done using 1.2 μ m fluorescent (637 nm/700 nm exc/em) polystyrene beads and 1 μ m slit pore membranes. A tangential flow through device⁵ was setup and beads were injected using a syringe pump at 25 μ L/min. Capture was completed over 5 minutes. Despite having a different setup, capture in this setup should be analogous to capture within a μ SiM-DX.



Video S.2: 1.24 μm bead capture on a 1 μm slit pore membrane is imaged on a confocal microscope. Fluorescence intensity increases over time as more beads are captured on the membrane.

Figure S.2: Single Virus Capture Analysis

Figure S.2 shows a number of viruses captured on a microslit membrane. It is recorded under a confocal microscope using a camera (2048 x 2048 pixel with a pixel pitch of 6.5 µm) and a 60X/1.2NA microscope objective. This configuration makes each pixel size approximately 108 nm since it is equal to the camera pixel pitch per the magnifying power of the objective. The dimension of a single virus is roughly 300 nm, and each virus emits at a wavelength of 633 nm. According to Abbe's diffraction limit, the spatial resolution of the optical system is almost 186 nm which is less than the virus dimension. In other words, each virus occupies an area of approximately 3 x 3 pixels on the image plane. These parameters can be used to detect single viruses on the membrane. To detect single viruses, the recorded image is first normalized, and then the threshold operation is applied. The threshold value can be empirically estimated by sweeping it between zero and one and then sequentially monitoring single viruses on the image. It is observed that the threshold value of 0.7 provides better results and detects single viruses around the clustered ones. Once the threshold operation is performed, the particles with an area of less than 3 x 3 pixels and higher than 4 x 4 pixels should be eliminated since a single virus roughly covers an area between these values. Figure S.2 illustrates the single viruses enclosed in blue boxes. A total number of 544 single viruses on the membrane are detected.

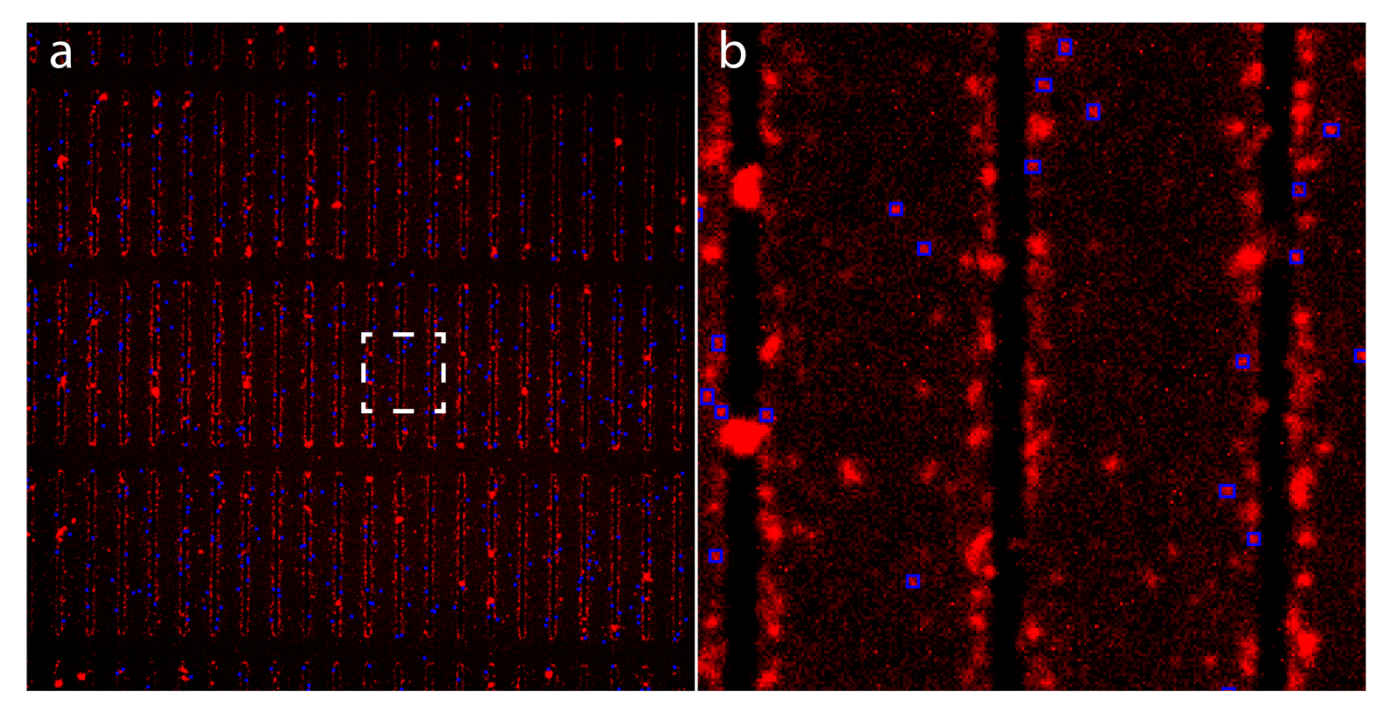


Figure S.2: The vaccinia virus that was captured from an injection of 40 μL of 3E9 virus/mL solution in a 1 μm slit pore μSiM-DX is analysed for the presence of single virus. Marked in blue boxes, there are 544 single viruses found in the entire image (a). The white box represents the zoomed in area shown in panel b (b).

Figure S.3: μSiM -DX Vaccinia Virus Dynamic Range

The dynamic range of the μ SiM-DX according to diagnostic sensitivity and specificity is represented on a vertical bar plot in Figure S.3. As in Figure 4, this shows that the 2 window μ SiM-DX has a lower dynamic range than the 3 window μ SiM-DX. Despite this, the dynamic range of both versions of the μ SiM-DX are complimentary to each other.

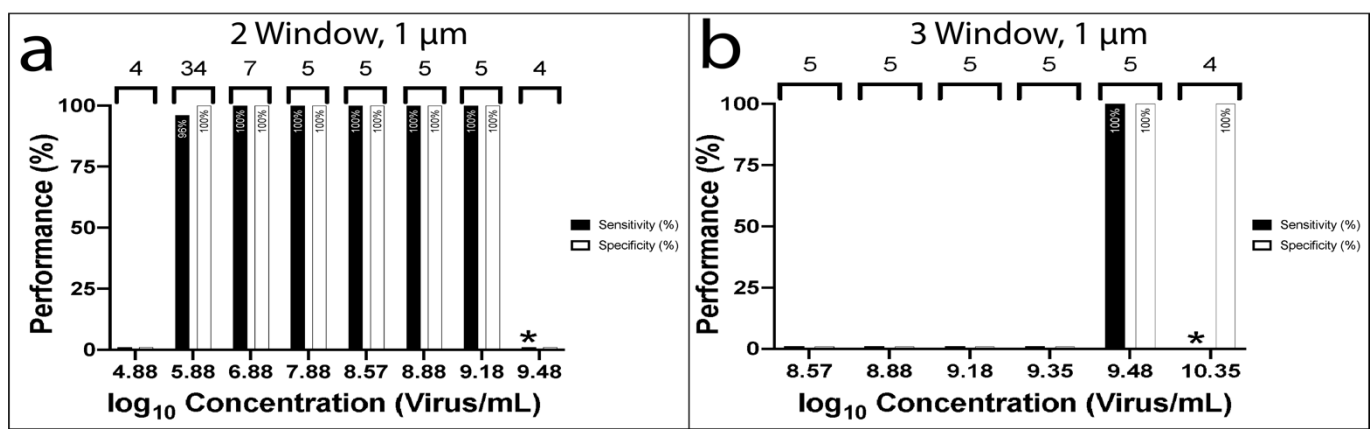


Figure S.3 The dynamic range of 2 window and 3 window 1 µm slit pore µSiM-DX are represented using diagnostic sensitivity and specificity (a, b). N values are shown above each data set. Asterisks denote undefined values due to a lack of true positives and false negatives.:

Figure S.4: DLS Size Distribution by Number for Intact and Sonicated Vaccinia Virus

Figure S.4 shows the size distribution by number for intact and sonicated vaccinia virus after analysis via DLS plotted on a semi-logarithmic scale. Three technical replicates are analysed and shown for both sample types.

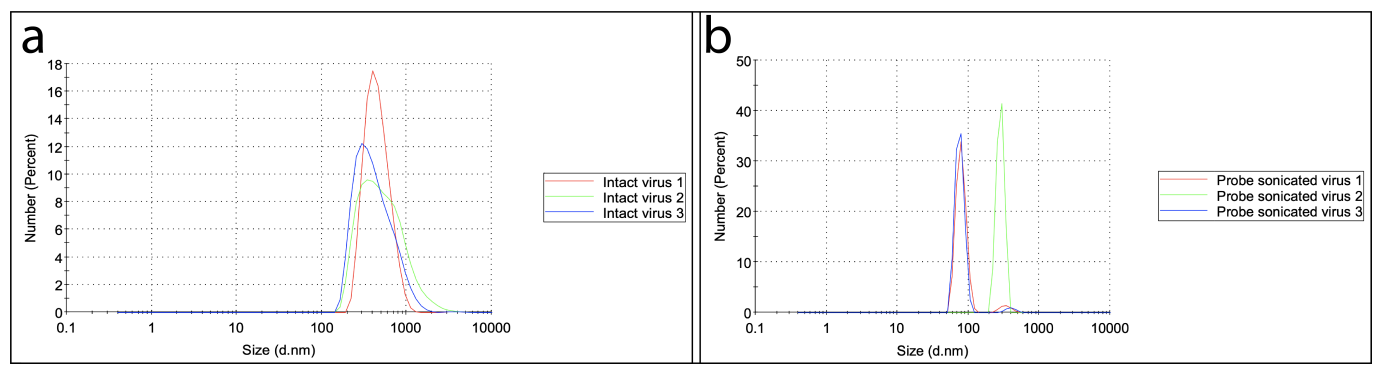


Figure S.4: Vaccinia virus is analysed using DLS and the resulting size distribution by number is shown for intact virus (a) and sonicated virus (b). Technical replicates are measured for each sample type. Size is displayed on a logarithmic scale along the x-axis according to the diameter of the measured particles.

Table S.1: Figure 2 Raw Data

μSiM-DX Version	Target	PBS (Switch/Total Tests)	Target capture (Switch/Total Tests)	False Positive (FP)	False Negative (FN)	True Positive (TP)	True Negative (TN)	N value	Sensitivity (TP/(TP+FN)	Sensitivity (%)	Specificity (TN/TN+FP)	Specificity (%)
0.5 μm	Steric Beads	2/3	8/10	2	2	8	1	13	0.80	80%	0.33	33%
	Affinity Beads		5/8	2	3	5	1	11	0.63	63%	0.33	33%
0.5 μm with a tube	Steric Beads	4/13	13/13	4	0	13	9	26	1.00	100%	0.69	69%
	Affinity Beads		8/10	4	2	8	9	23	0.80	80%	0.69	69%
3 slot, 1 μm	Steric Beads	0/7	5/7	0	2	5	7	14	0.71	71%	1.00	100%
	Affinity Beads		2/3	0	1	2	7	10	0.67	67%	1.00	100%
2 slot, 1 μm	Steric Beads	0/3	7/7	0	0	7	3	10	1.00	100%	1.00	100%
	Affinity Beads		7/7	0	0	7	3	10	1.00	100%	1.00	100%

Table S.2: Figure 4 Raw Data

log Concentration (virus/mL)	PBS - (Switch/Total Tests)	Vaccinia - (Switch/Total Tests)	Vaccinia + Vaccinia Ab - (Switch/Total Tests)	Vaccinia + Rabbit Ab - (Switch/Total Tests)	False Positive (FP)	False Negative (FN)	True Positive (TP)	True Negative (TN)	N value	Sensitivity (TP/(TP+FN)	Sensitivity (%)	Specificity (TN/TN+FP)	Specificity (%)	
	3 slot, 1 μm													
8.57		0/1	0/1	NA	0	1	0	4	5	0.00	0%	1.00	100%	
8.88	0/3	0/1	0/1	NA	0	1	0	4	5	0.00	0%	1.00	100%	
9.18		0/1	0/1	NA	0	1	0	4	5	0.00	0%	1.00	100%	
9.35		0/1	0/1	NA	0	1	0	4	5	0.00	0%	1.00	100%	
9.48		0/1	1/1	NA	0	0	1	4	5	1.00	100%	1.00	100%	
10.35		0/1	NA	NA	0	0	0	4	4	Undefined	Undefined	1.00	100%	
				2 s	slot, 1 μm									
4.88		NA	0/1	NA	0	1	0	3	4	0.00	0%	1.00	100%	
5.88		0/3	24/25	0/3	0	1	24	9	34	0.96	96%	1.00	100%	
6.88		0/1	3/3	NA	0	0	3	4	7	1.00	100%	1.00	100%	
7.88		0/1	1/1	NA	0	0	1	4	5	1.00	100%	1.00	100%	
8.57	0/3	0/1	1/1	NA	0	0	1	4	5	1.00	100%	1.00	100%	
8.88		0/1	1/1	NA	0	0	1	4	5	1.00	100%	1.00	100%	
9.18		0/1	1/1	NA	0	0	1	4	5	1.00	100%	1.00	100%	
9.48		1/1	NA	NA	1	0	0	3	4	Undefined	Undefined	0.75	75%	

Table S.3: Figure 5 Raw Data

PBS (Switch Tes	/Total	Intact Vaccinia	Sonicated Vaccinia	False Positive (FP)	False Negative (FN)	True Positive (TP)	True Negative (TN)	N value	Sensitivity (TP/(TP+FN)	Sensitivity (%)	Specificity (TN/TN+FP)	Specificity (%)
0/	3	3/3	0/10	0	0	3	13	16	1.00	100%	1.00	100%

Table S.4: Total Vaccinia Test Data

PBS - (Switch/Total Tests)	Vaccinia - (Switch/Total Tests)	Vaccinia + Vaccinia Ab - (Switch/Total Tests)	Vaccinia + Rabbit Ab - (Switch/Total Tests)	Sonicated Vaccinia	False Positive (FP)	False Negative (FN)	True Positive (TP)	True Negative (TN)	N value	Sensitivity (TP/(TP+FN)	Sensitivity (%)	Specificity (TN/TN+FP)	Specificity (%)
0/6	0/10	32/33	0/3	0/10	0	1	32	29	62	0.97	97%	1.00	100%

References

- 1. E. Korchagina, A. Tuzikov, A. Formanovsky, I. Popova, S. Henry and N. Bovin, Carbohydrate research, 2012, 356, 238.
- 2. E. Williams, K. Barr, E. Korchagina, A. Tuzikov, S. Henry and N. Bovin, *International journal of molecular sciences*, 2016, **17**, 118.
- 3. L. Deng, E. N. Kitova and J. S. Klassen, Journal of the American Society for Mass Spectrometry, 2013, 24, 49-56.
- 4. J. P. Landry, Y. Ke, G.-L. Yu and X. D. Zhu, Journal of immunological methods, 2015, 417, 86-96.
- 5. M. Dehghani, K. Lucas, J. Flax, J. McGrath and T. Gaborski, *Advanced materials technologies*, 2019, **4**, 1900539-n/a.